Journal of The Electrochemical Society

The Electrochemical Society
Advancing solid state & electrochemical science & technology

OPEN ACCESS

Neutron Imaging Experiments to Study Mass Transport in Commercial Titanium Felt Porous Transport Layers

To cite this article: H. Altaf *et al* 2023 *J. Electrochem. Soc.* **170** 064507

View the article online for updates and enhancements.

You may also like

- Effects of the Transport/Catalyst Layer Interface and Catalyst Loading on Mass and Charge Transport Phenomena in Polymer Electrolyte Membrane Water Electrolysis Devices
J. Lopata, Z. Kang, J. Young et al.

- Polymer Electrolyte Water Electrolysis: Correlating Porous Transport Layer Structural Properties and Performance: Part I. Tomographic Analysis of Morphology and Topology
Tobias Schuler, Ruben De Bruycker, Thomas J. Schmidt et al.

- Three-Dimensional Anisotropic Electrical Resistivity of PEM Fuel Cell Transport Layers as Functions of Compressive Strain
Devin Todd, Maximilian Schwager and Walter Mérida

We Advance Battery Research!

EL-CELL®
electrochemical test equipment

- Electrochemical Battery Test Cells
- Multi-channel Potentiostats / Galvanostats / EIS
- Tools, Consumables & Testing Services

el-cell.com +49 40 79012-734 sales@el-cell.com

This content was downloaded from IP address 193.175.53.21 on 17/10/2023 at 14:03

Journal of The Electrochemical Society, 2023 **170** 064507

Neutron Imaging Experiments to Study Mass Transport in Commercial Titanium Felt Porous Transport Layers

H. Altaf,[1,2,z] T. Milicic,[2] T. Vidakovic-Koch,[2] E. Tsotsas,[1] Alessandro Tengattini,[3] N. Kardjilov,[4] T. Arlt,[4] I. Manke,[4] and N. Vorhauer-Huget[1]

[1]*Otto von Guericke University, Institute of Process Engineering, 39106 Magdeburg, Germany*
[2]*Electrochemical Energy Conversion Group, Max Planck Institute for Dynamics of Complex Technical Systems, 39106 Magdeburg, Germany*
[3]*Institut Laue-Langevin, 38000 Grenoble, France*
[4]*Institute of Applied Materials, Helmholtz Zentrum Berlin, 14109 Berlin, Germany*

In this work, neutron imaging was used to visualize and study invasion phenomena in fibrous porous transport layers (PTLs) of titanium felt under different flow conditions of gas and liquid phase. The experiments were realized with flow cells that contained a gas and a liquid flow channel separated by PTLs with different thicknesses and pore size distributions. The invasion can be characterized by counter-current flow of water and air with joint imbibition and drainage processes. The dynamics were visualized with neutron radiography with a local resolution of 6.5 μm and a temporal resolution of 0.1 s. Individual static gas-liquid distributions were additionally studied by neutron tomography, with a local resolution of 22 μm and an exposure time of 1.5 s per image (projections: 800/360°). It is shown and discussed that the invasion occurred in continuously repeated imbibition/drainage cycles with frequencies depending on the flow conditions and the PTL structure as well. The change of the PTL saturation with air or water appeared almost independent from the specific PTL structure and the breakthrough of the gas phase occurred at almost constant positions.

© 2023 The Author(s). Published on behalf of The Electrochemical Society by IOP Publishing Limited. This is an open access article distributed under the terms of the Creative Commons Attribution 4.0 License (CC BY, http://creativecommons.org/licenses/by/4.0/), which permits unrestricted reuse of the work in any medium, provided the original work is properly cited. [DOI: 10.1149/1945-7111/acd7a8]

Manuscript submitted January 11, 2023; revised manuscript received May 15, 2023. Published June 21, 2023.

The two-phase mass transport within the porous transport layer (PTL) of proton exchange membrane water electrolysers (PEMWE) is crucial for the efficiency of the system. It is shown by experiments,[1–6] that various parameters, for example, porosity of the PTL, its thickness and pore size distribution (PSD) as well as the stoichiometry of the fluid flow have a great influence on the counter-current transport of gas and liquid. However, exact correlations and a proper understanding is still lacking due to complex experimental designs and the coupling of several process parameters with each other. Different modeling techniques[7–12] have therefore been developed to study the transport mechanisms at various scales. The experimental validation of these models is challenging, mainly due to the complexity of a PEMWE, where there are various limitations to measure or to visualize two-phase mass transport.

Experimentally most promising are in-operando methods which are suitable to visualize and quantify two-phase transport under operating conditions.[13–19] Most experimental approaches are based on 2D in-plane radiographic visualization of the whole PEMWE or of microfluidic cells that capture only the mass transfer at the anode side.[15,16,18] In-plane means that the cross-section of the PTL between water flow channel and catalyst layer or gas channel is visualized. From this, the accumulated information about the distribution of gas along the height of the PTL is obtained. In other studies,[17,19] instead through-plane imaging was applied. In this, the PTL is visualized along the horizontal cross section, thus accumulating the gas and liquid distribution between its top and bottom side. In contrast to in-plane studies, this visualization allows to investigate the spatially distributed breakthrough of oxygen along the water flow channel. In addition to that, tomographies were also conducted.[20]

The displacement through PTLs is said to be capillary dominated[13] and influenced by the PTL structure.[13,21,22] In addition to that, Shojaei et al.[23] observed that the fluid menisci form minimal surfaces between hydrophilic and hydrophobic parts of fibrous porous media. These surfaces have no pressure difference between liquid and gas phase which ensure continuity of flow regardless of the flow regime. Lin et al.[24] also addressed the existence of such minimal surfaces which imply that the existence of well-connected phases within the porous medium. Furthermore, Armstrong et al.[25] showed that a macroscale value of capillary number (Ca), rather than a microscale one, correctly describes the mobilization of non-wetting phase. They argue how the Ca for a system would change with the size of the system and to assume that the viscous and capillary forces act over the same lengths scales can be problematic. In another study[26] they show that the that the capillarity also acts in a non-local way like viscous forces. Ferrari et al.[27] reported that even in capillary dominated regimes, the interaction of viscous, inertial and capillary forces, result in complex flow regimes depending on the geometry. This is true for porous materials like PTLs with complex geometries to resolve. The spatial distribution of the wettability is much more complicated to determine. Using multi-phase flow experiments, Garfi et al.[28] created a pore based wetting index to characterize the wetting state of the porous medium. Such 3D maps can then be used as an input to pore scale models for a better understanding of a porous material.

In most situations studied in literature, gas-liquid distributions were independent of the operating parameters.[13,15,16] For example, in a study with a sintered PTL with an active area of 1 cm^2 (porosity 30% and thickness 1.2 mm) and in-plane configuration (operating temperature 50 °C and pressure 2 bar), Seweryn et al.[15] found that the distribution of oxygen and water is unaffected by the flow variations and current densities which varied from 0.1 to 2.5 A cm^{-2}. Additionally, no water scarcity in the PTLs was reported. Satjaritanun et al.[20] used X-ray tomography (μ-CT) to study the oxygen pathways through the PTL in an electrolyser that was operated at 1 and 4 A cm^{-2}. They used two carbon paper gas diffusion layers (GDLs) treated as anode PTLs. The porosity profile showed an average porosity of the PTL between 30–40%. They observed that oxygen takes certain preferential pathways through the PTL regardless of the water flowrate and current density. Similarly, Zlobinski et al.[13] explored a wide range of current densities (0.1–2.0 A cm^{-2}) and pressure conditions (1–8 bar) as well at a constant temperature of 50 °C. They showed that the flow within the sintered PTL (1 mm thick, unknown porosity) is completely capillary driven and that the increased mass transport losses might possibly be due to the interface between the PTL and the catalyst coated membrane (CCM). This outcome was explained with independence of saturation profiles inside the PTL on current density and pressure

[z]E-mail: haashir.altaf@ovgu.de

variations. They concluded that hydrophobic regions in the PTL actually prevent the complete wetting of the PTL and hence promote the gas pathways, while also leading to local gas entrapments. Selamet et al.[19] investigated two-phase transport using through-plane neutron imaging. They performed experiments at lower current densities (0.1 and 0.4 A cm^{-2}) and at two different temperatures i.e. 25 and 40 °C. They used a 1 mm thick PTL with a porosity of 44%. They showed that the water distribution was impacted by the proximity to the inlet and outlet channels as well as gravity and buoyancy forces. Furthermore, they observed the periodic release of gas bubbles from the same spots during the operation. At the same time, they also showed that various stagnant regions exist in the PTL which do not contribute to the imbibition of water. This was confirmed in Panchenko et al.,[16] where various stoichiometries (between 95 and 1037) were realized in a non-electrochemical cell to investigate in more details the gas-liquid distribution. It was found that gas bubbles always exit from the same location, independent of the flow conditions, and that 37% of the pore volume could not be wetted by water.

In contrast to these examples, it was shown that the PTL invasion and gas-liquid distribution also depend on flow conditions. For example, Maier et al.[17] demonstrated that increasing current density can decrease the water thickness. They combined μ-CT and neutron radiography to investigate the structural dependence of mass transport in PTLs. They used the through-plane configuration to compare three different PTLs with different structural properties. They used a sintered PTL (29.5% porosity, 2 mm thick) and two felt PTLs (47.1% porosity, 1 mm thick and 76.9% porosity, 0.1 mm thick). The cell was operated up to 1.5 A cm^{-2} and with an inlet water temperature of 50 °C. They observed a decrease in water thickness in the PTL with an increase in the current density. Moreover, in another study[17] it was comprehended that there is significant inhomogeneity in water thickness across the active area of the PTL—water thickness was higher where the flow velocity was higher in the flow channels. This showed a connection between the geometry of the field and the two-phase flow in the PTL.

Additionally, Hoeh et al.[29] used in-operando synchrotron X-ray imaging. They concluded that more pathways for gas transport are established with an increasing current density. Similarly, Panchenko et al.[30] reported that at higher current densities the gas is not drained properly and blocks the pathway of water to the catalyst layer. They operated their cell between 0.1 and 1 A cm^{-2} and used sintered titanium (Ti) PTL at the anode. This was confirmed by Lee et al.[18,31] who applied current densities between 2–9 A cm^{-2} and used a sintered Ti-PTL with 35% porosity, 0.25 mm thickness and an active area of 0.8 cm^2. They reported that especially at high current densities, the gas accumulates at the catalyst layer and blocks the pathway of water. They found that gas accumulation led to a 6% increase in the overpotential of the cell.[31]

As a result of these studies, e.g. Panchenko et al.[30] suggested to use a stoichiometry value greater than 100 since at lower stoichiometries, water starvation becomes a problem. At the same time, in order to mitigate potential losses caused by water starvation, Lee et al.[18] suggested to realize turbulent water flow through the PTL based on the observation that turbulent water flows are in favor for efficient gas removal at high current densities. Also Maier et al.[17] reported that a major volume of pores remained unused during operation due to the poor water intake of the PTLs and suggested that much more work should go into the design of novel PTLs which can increase the pore utilization.

This literature overview shows, although it is very convenient to study mass transfer through the PTLs with the help of μ-CT and neutron imaging, there are still a number of open questions to be addressed in order to gain a proper and full understanding of the mass transfer limitations. Since not many studies are available so far on this topic, the derived picture is not very clear, especially as the scarce data is often contradicting and not well related with the process parameters and the cell design. In brief, it remains unclear how the structural properties of the PTL need to be designed for different fluid flow conditions. So far, a clear recommendation for optimal structural properties to improve mass transport while conductivity and mechanical stability are at least sustained, is still missing. Instead, most of the studies neglect the structural characteristics or PTLs have been compared to each other only based on the difference in their bulk properties (i.e. porosity, thickness).[13,15,19,20,22]

In this work, we employed neutron imaging to study the water-gas distributions in various commercial felt PTLs with different structural parameters, namely thickness and pore size distribution, at different flow conditions. Neutron imaging is preferred over X-ray imaging because of the high attenuation by the titanium PTL in the X-rays and poor contrast between water and titanium. Even in neutron imaging, a complex experimental setup with several components puts a limit on the size of the region of interest investigated and as well as the image quality. It is also important to state here that the purpose of this study is not to study the physics of the pore scale invasions but rather the effect of structure and flowrates on the invasion patterns of different PTLs. For this purpose, a non-electrochemical flow cell, similar to the one reported by Panchenko et al.[16] was used in this study. Through-plane and in-plane radiographies as well as tomographies were conducted. For the through-plane visualization we made use of the advantage that the flow cell only represented the flow on the anode side. The through-plane imaging allowed us to study the filling characteristics, i.e. the imbibition of water, and water retention, i.e. its drainage by air, with the according spatial dependence along the flow channels. The goal of this work is to show that both, flow conditions and structure, affect the gas-liquid distribution inside the PTL, and that the structure of the PTL cannot be optimized independently of the flow conditions.

Experimental

Neutron imaging.—All of the experiments were performed at the high flux (1.4×10^{10} n cm^{-2}/s) beam line NeXT[32] at Institut Laue-Langevin (ILL), Grenoble, France. The high-resolution detector was employed, with a 20 μm thick Gadox scintillator, 50 mm f./1.2 Canon imaging lens, 55 mm f./1.0 objective lens, and Hamamatsu ORCA-Flash V3 sCOMS camera. The field of view was 14.64×14.64 mm^2, the distance from the detector was 12 mm and a pixel size of 6.5 μm was obtained. Radiography images were recorded with a temporal resolution of 10 s^{-1}. For tomography, the gas-liquid distribution was stabilized by tightening of screw clamps at all inlet and outlet ports of the cell. The tomographies were then conducted with an exposure time of 1.5 seconds with 800 projections per 360° rotation and a distance of 15 mm from the detector. A resolution of 22 μm was obtained for all tomographies. A compromise had to be made between the contrast, domain size and the resolution. The spatial resolution used is too low to visualise individual pore invasions but good enough to resolve distinct breakthrough regions on a relatively larger domain. In this way, it was possible to use a bigger domain size in comparison to previous studies mentioned in the literature review. Similarly, for the time resolution, 0.1 s was found to be sufficient for observing the invasion/imbibition cycles for all the three PTLs used. The associated time scales for pore scale drainage (or Haines jumps) are much shorter to be observed with 0.1 s resolution.

Cell design.—The schematic illustration of the flow cell is shown in Fig. 1. It was designed similarly to Panchenko et al.[16] but with some modifications. The cell used in our study was designed for through-plane imaging with the plane view of the PTL facing towards the neutron source. For this reason, the shape of the cell was more elongated with flow inlets and outlets at the top rather than on the sides of the cell. This was also advantageous for tomography measurements; the inlets and outlets at the top made it convenient to rotate the cell without tangling the pipes during rotation. The cell body, the screws and connectors were made from aluminum. Teflon was used for sealing of the water channel and the PTL. As shown in

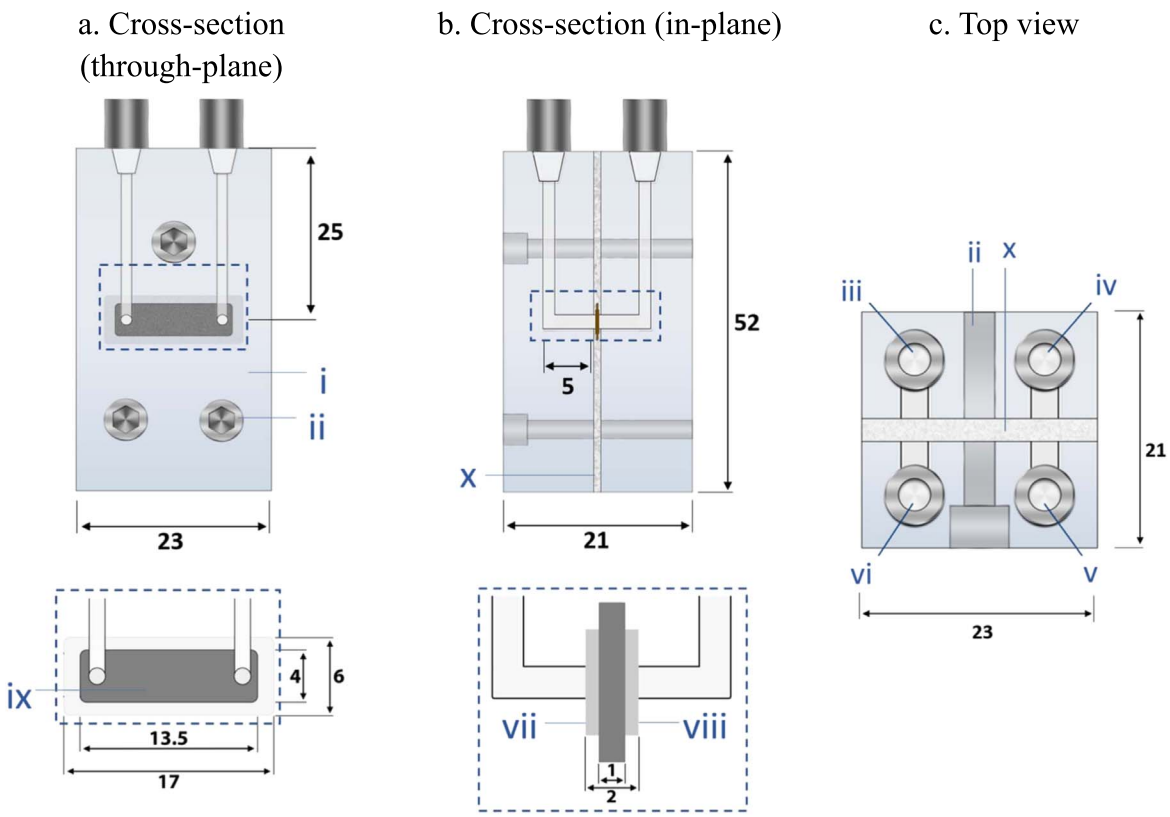

Figure 1. Design of the flow cell and dimensions: a) cross-section of through-plane view; b) cross-section of in-plane view; c) top view. i - cell housing; ii - connection screws; iii - water inlet; iv - water outlet; v - air inlet; vi - air outlet; vii - air supply channel; viii - water supply channel; ix - PTL; x - Teflon sealing.

Fig. 1, the cell had two channels which were 0.5 mm thick, 4 mm wide and 13.5 mm long. The PTL was placed in between these channels with an active area of 13.5 mm by 4 mm (Fig. 1). Each channel was connected to an inlet and outlet and is attributed to water or air side, respectively.

Experimental setup.—The cell was used for through-plane and in-plane radiographies and tomographies. While the through-plane radiographies and tomographies were used to study the dependence of invasion process on PTL structure and flow conditions, the in-plane visualization was only employed to monitor the transport of fluids through the supply channels.

The cell was positioned very close to the detector to enable a high local resolution (Fig. 2). The distance between cell and detector was 12 mm during radiography imaging, thus allowing a high spatial resolution of 6.5 μm. The visualized region of interest (ROI) had a smaller cross section than the actual PTL, namely 9.5 $\times$ 4 mm^2, which is indicated in Fig. 2. The distance of the cell to the detector was 15 mm during tomography imaging, i.e. enabling the rotation of the cell and thereby compromising in resolution, which was 22 μm.

Two syringe pumps from World Precision Instruments Germany GmbH (continuous flow pumps with dispensing accuracy of ± 1%) were used for water and air supply. With these pumps non-oscillating fluid supply could be realized. They were located approximately 80 cm away from the cell to avoid radioactive activation during the measurements. The connecting polyethylene pipes had an inner diameter of 2 mm. Screw clamps (stainless steel) were used to close the pipes during different types of operations.

PTL materials.—Three cells were prepared for the experiments, each one containing a different commercial Ti-felt PTL (Table I). Besides the thickness, the PTL parameters varied in terms of porosity and pore size distribution (Table I). Moreover, the PTL from Sylatech had a graded structure, with smaller pores on the gas channel side and larger pores at the water channel side. In addition to that, it had previously been used in PEMWE prior to the neutron imaging experiments and the thickness had been reduced by 0.15 mm due to compression. This means that the thickness of PTL 1 in neutron imaging experiments was 0.85 mm.

Experimental parameters.—Air and deionized water (H_2O) were used for these experiments. The air mass flow rates and the water mass flow rates given in Table II were calculated using Faraday's law:

$$\dot{M}_i^F = \frac{\tilde{M}_i \cdot I}{z_i \cdot F}, \quad [1]$$

for i = H_2O, O_2 and with Faraday constant F = 96485 A s mol^{-1}, charge number z = 4 for the gas phase and z = 2 for water, molecular weight $\tilde{M}_{O_2}$ = 32 g mol^{-1} or $\tilde{M}_{H_2O}$ = 18 g mol^{-1}, and current I in A,

$$I = j \cdot A, \quad [2]$$

with current density j provided in Table II and surface area A = 54 mm^2.

The stoichiometry λ is defined as the ratio of the volume flow rate of water supplied to the experiment, $\dot{V}_{H_2O}^{exp}$, to the required amount of water consumed in the reaction, $\dot{V}_{H_2O}^F = \rho_{H_2O}^F / \dot{M}_{H_2O}^F$, calculated by Eq. 1:

$$\lambda = \frac{\dot{V}^{exp} \cdot \rho_{H_2O}^F}{\dot{M}_{H_2O}^F} \quad [3]$$

For each cell, different operation scenarios were carried out: filling (water imbibition into the previously empty PTL), counter-

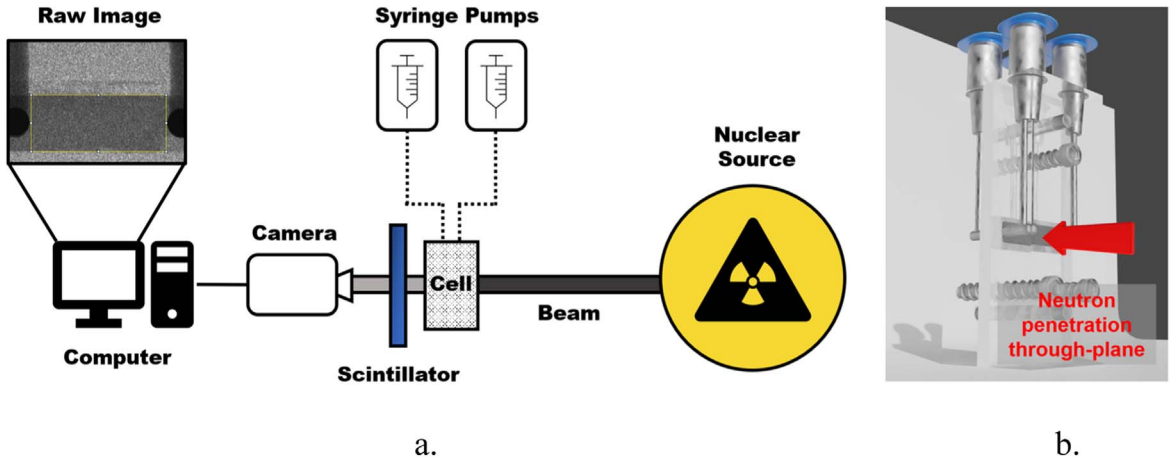

Figure 2. (a) Schematic diagram of the experimental setup. (b) Cell orientation in the through-plane view set-up.

Table I. list of PTLs used in experiments and their properties as provided by the manufacturer.

PTL Producer	Producer data		
	Thickness, mm	Uncompressed porosity, %	Av. fiber diameter, μm
Sylatech (PTL 1)	1.000	80	30-45
Bekaert (PTL 2)	0.500	77	20
Bekaert (PTL 3)	1.000	77	20

Table II. Flow settings used for each cell. CC: Counter-current flow of liquid and gas.

Flow settings	H2O flow rate, ml min^{-1}	Air flow rate, ml min^{-1}	Stoichiometry	Corresponding current density, A cm^{-2}
Filling	0.05-1.000	—	—	—
CC-Setting 1	0.582	3.950	100	2.00
CC-Setting 2	2.183	9.874	150	5.00
CC-Setting 3	3.056	13.823	150	7.00
CC-Setting 4	3.929	17.773	150	9.00
Drainage	—	7.9	—	—

current (CC) flow of air and water as well as drainage (Table II, Fig. 3). During filling, the gas channels were closed on both sides (inlet and outlet) using the screw clamps and the water was supplied at constant flow rate as given in Table II. For CC flows, four settings were chosen corresponding to different overall flow rates of air and water. Only the gas exit valve was closed during CC operation to enable pressure build-up at the gas side. In the drainage setting, both, the water inlet and the gas outlet were closed to allow a higher-pressure build-up and higher air occupancy in the PTL domains.

Image processing.—All image processing steps were performed with ImageJ (Version 2.1051). Dark-field (DF) and dry-cell images (DC) were used to normalize the sample images. For this purpose, DF median images were subtracted from the sample images (M) and

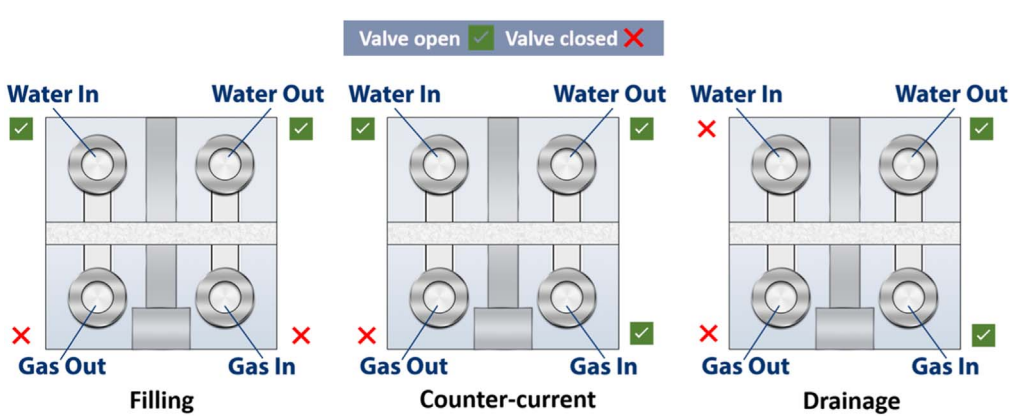

Figure 3. Three different operating scenarios used in the experiments for each PTL. The green checks identify the open valves; red crosses identify closed valves.

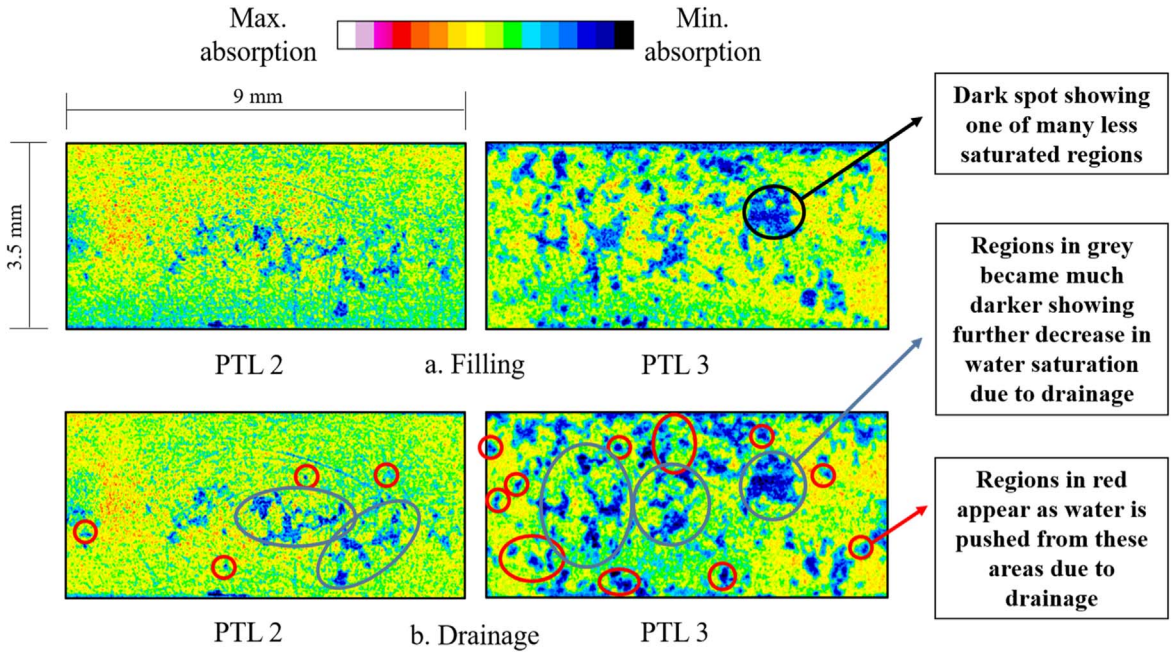

Figure 4. Center images from the 3D image stacks obtained by tomography of PTL 2 (left) and PTL 3 (right) after a. filling and b. drainage (through-plane view). The spatial resolution is 22 μm. (Note: The tomography for PTL 1 was not performed due to the limited beam time allocation at the ILL, Grenoble).

also from the median of DC images. By that, the grayscale deviations, which might have been caused by sensitivity of the CCD camera and the detector, were accounted for and thus images (T), Eq. 4, that contain just the information about water distribution —without the Ti fibers—were obtained.

$$T = \frac{M - DF}{DC - DF} \quad [4]$$

As the images were taken with a frame rate of 10 s^{-1}, the change of the transmission T can be investigated with high temporal resolution. The change of water saturation inside the cell can then be correlated with a change of the transmittance signal. Higher transmission values are correlated with more air in the image and lower transmission means more water.

The water thickness is obtained from Eq. 5, i.e. after normalizing it by the information of the completely dry cell and Beer-Lambert law (BLL). It is the total amount of water in the neutron beam.

$$d = \frac{lnT}{-\mu} \quad [5]$$

Here, μ is the attenuation coefficient of water (approx. 0.5 mm^{-1})[29] and d is the water thickness. In the through-plane view, the thickness comprises the water inside the water channel, with a thickness of 0.5 mm, as well as the water contained in the PTLs, with thicknesses varying between 0.5 mm and 1 mm and porosities specified in Table I. Gas bubbles, both inside the PTL and the water channel, and Ti fibers reduce the overall water thickness in through-plane view direction.

The average water thickness $\bar{d}$ is computed for all images taken during steady-state operating conditions of each experiment as a function of the horizontal distance s. The average water thickness $\bar{d}(s)$ comprises the data from all image pixels along the vertical height of the image at space coordinate s. The global minimum water thickness in space indicates the breakthrough location of the gas phase of each experiment.

Results and Discussion

Tomography of water imbibition into empty cells.—For this study, the empty PTLs were at first completely flooded with water (0.05-1.000 ml min^{-1}) for 3-4 min before the tomography was performed. The water inside the cells was stabilized by closing the screw clamps. Figure 4 shows the center slice of the obtained 3D image stacks in through-plane view for PTL 2 (thickness 0.5 mm) and PTL 3 (thickness 1 mm). Due to the big difference in the mass attenuation coefficients of air and Ti it is possible to differentiate between these materials: For a mean neutron energy of 12.3 meV, the normalized mass attenuation coefficients (σ/ρ in g cm^{-2}) are very similar but since the density of air (0.001225 g cm^{-3}) is much lower than that of Ti (4.5 g cm^{-3}), the latter absorbs much more neutrons than air. The contrast is proportional to the density difference of the materials.[33]

Anticipating that the dark areas and black spots refer to large pores, one can conclude that both of the PTLs show a very non-uniform water uptake. In the case of the thinner PTL 2 (Fig. 4a) only a few dark regions are observed. The thicker PTL (Fig. 4b.) has much more dark regions as a result of less absorption by the gas phase. These regions identify structures in the PTL where the imbibition of water was limited. This indicates local water scarcity in both PTLs, similarly as already reported in Ref. 17. In both cases, these regions are distributed throughout the PTLs. It can be anticipated that such a phenomenon also occurs in the PTLs during PEMWE. For the case of dynamic operation of a PEMWE it is therefore of great interest how these gas islands depend on structure and operating conditions, how long they remain and if they impair mass transfer through the PTL. Repetition of the tomography after purging the cells with air at a flow rate of 7.9 ml min^{-1} for approximately 5 min did reveal that the gas islands remained. They partly grew and merged with other unsaturated regions. This shows that water scarcity can be an issue for transport limitations also under dynamic conditions, i.e. repeated imbibition/drainage cycles, which deserves further investigations as this impacts the relative liquid and gas permeabilities.

Radiography of counter-current flow with different stoichiometries.—The dynamic change of water and air saturation during the CC settings are studied based on radiographies which were taken with a frame rate of 10 s^{-1}. Based on the image data and Eq. 4, the temporal change of the average transmittance can be illustrated. It is shown for the example of PTL 2 and setting 4 in Fig. 5. The change

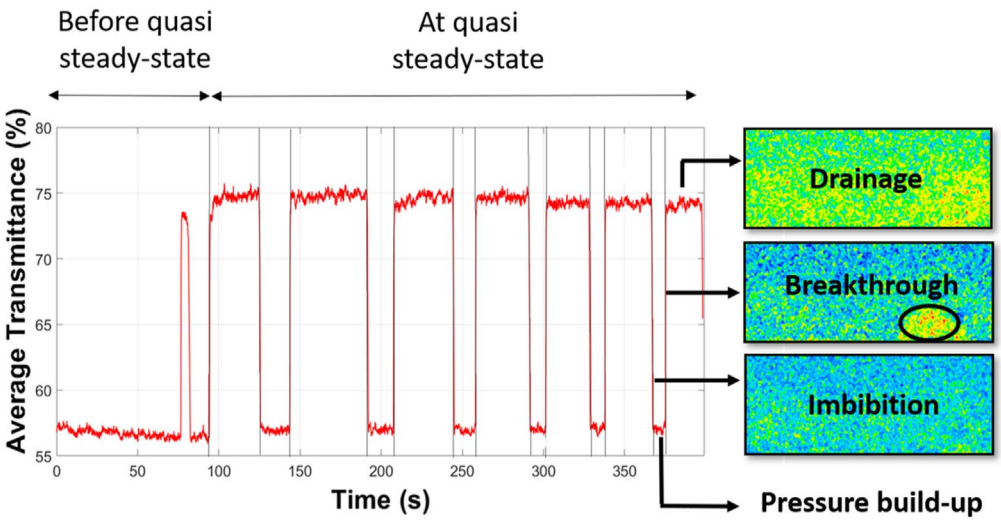

Figure 5. Illustration of periodic change of the average transmittance of neutron radiation following imbibition/drainage cycles with constant frequency and amplitude. Here the example of PTL 2 at setting 4 is shown.

of the average transmittance corresponds to the change of the water or air saturation in the through-plane view, i.e. inside the PTL and the channels. High values of the average transmission correspond to the situation with less water inside PTL and channels and low values correspond to a higher water content.

As can be seen in Fig. 5, the average transmittance changes periodically which indicates a periodic change of the through-plane saturation, similarly as already reported by Selamet et al.[19] for PTLs and also by Mularyzyk et al.[34] for GDLs. It can thus be concluded that imbibition and drainage of water by air repeated periodically in imbibition/drainage cycles. At the lower average transmission levels (at around 57%) the water saturation inside PTL and channels remained constant. During these periods, approximately 12.6 s long in Fig. 5, the air pressure was build-up inside the gas channels until reaching the critical invasion pressure threshold of the PTL. Then, drainage occurred instantly when the average transmission changed from the lower to the upper level (at around 75%). This is also referred to the breakthrough of the gas phase. The saturation remained constant for an almost constant interval of 32.7 s on average while the gas phase was released. During this period, air was continuously removed from the gas channel. The released gas bubbles replaced the water in the liquid channel in its flow direction, thus affecting the average transmittance of the 2D through-plane image. The image from the drainage period in Fig. 5 appears therefore overall much brighter. After pressure equalization between the gas and the liquid channel, this process stopped and the gas was again replaced by water due to imbibition. This is identified by the change of the average transmission from the upper to the lower level in Fig. 5, which also occurred instantly. However, from the radiography images (as exemplarily shown in Fig. 6) it does not become clear if full saturation of the PTL was again achieved. The average transmission plots in Figs. 5 and 6 suggest that the initial neutron transmission was obtained after each cycle, indicating that a similar water saturation of the channel and the PTL was yielded after every drainage cycle.

After imbibition, the gas pressure build-up period was repeated with a steady frequency and amplitude of the interval. The frequency of this cycle is 0.0214 s^{-1} and the amplitude change is 17.4% in the example shown in Fig. 5.

The quasi steady-state imbibition/drainage cycles were observed in all settings and PTLs studied here. The frequencies and amplitudes of these cycles are provided in Fig. 7 and Table III. As can be seen, steady conditions were achieved later in the experiments with low flow rates, because air bubbles inside the water supply channel affected the experiments at the start. This disturbance stopped earlier in cases with higher flow rates. In brief, the low flow rates in setting 1 affected the frequencies and amplitudes of the imbibition/drainage cycles, which were not as well established as in settings 2-4. It is expected that this behavior impaired the mass transfer through the PTL in case of the low flow rates.

It is generally expected that higher gas flow rates would result in shorter time periods of pressure build-up, because simply the pressure inside the gas channel could build-up faster. This is only partly reflected by the measurement data in Table III. Deviations from the quasi steady-state imbibition/drainage profiles in Fig. 6 yield high standard deviations in Table III, which are in the range of the expected change of the parameter. At the same time, the water flow rates were increased with rising gas flow rates, resulting in higher invasion pressure thresholds of gas draining liquid filled pores and throats of the PTLs. Accordingly, longer drainage periods are expected for higher gas flow rates, because more gas has to be released.

Interestingly, PTL 1 has overall shorter pressure build-up periods than the other two PTLs, especially at low gas and liquid flow rates. This might be due to larger pores towards the water-channel side in the graded PTL and thus a result of the specific PTL structure.

Apart from that, the following picture can be derived from Figs. 6 and 7 and, Table III. The frequency of the cycles seems to depend on both, the PTL structure and the process conditions (fluid flow rates and resulting fluid pressure differences). As can be seen, in case of PTL 1, which is a graded PTL, the impact of flow conditions is much more significant than for the other two cases. Though, the impact is still higher in case of the thin PTL 2 than for the thicker PTL 3, where the flow conditions have almost no impact on the frequency. The variation of the transmittance value instead is only small between settings 2–4 and the different PTLs (Fig. 7b). In brief, when associating the average transmittance with air saturation, it could be concluded that in all PTLs a similar saturation was obtained, at least in settings 2–4. This means that the overall air occupation seemed almost independent of the PTL structure and flow conditions. This is in agreement with results reported in Refs. 13,15,19. However, the transmittance values are accumulated values over the whole through-plane view, thus incorporating information about the channel saturations, too. This could blur the transmittance information of the PTLs. As shown in Fig. 8, the occurrence of gas bubbles inside the water channel can affect the through-plane data. Further investigations, incorporating in-plane visualization of the PTL saturation would therefore be recommended. In the current study, the strong absorption of neurons in in-plane direction did not allow for an estimation of saturation profiles in this direction.

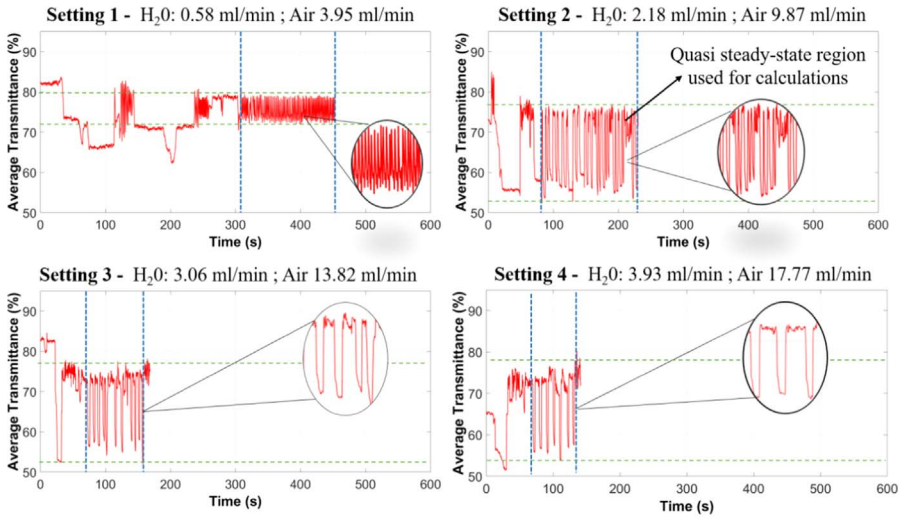

a. PTL 1

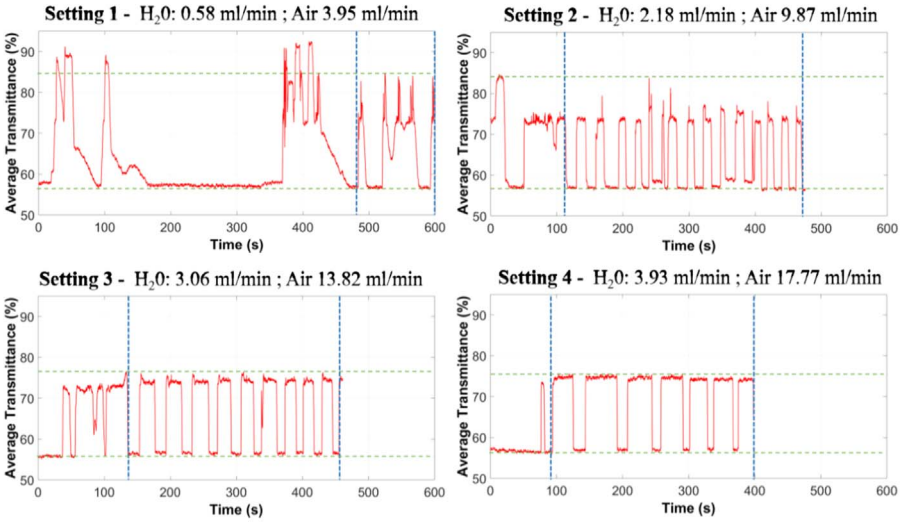

b. PTL 2

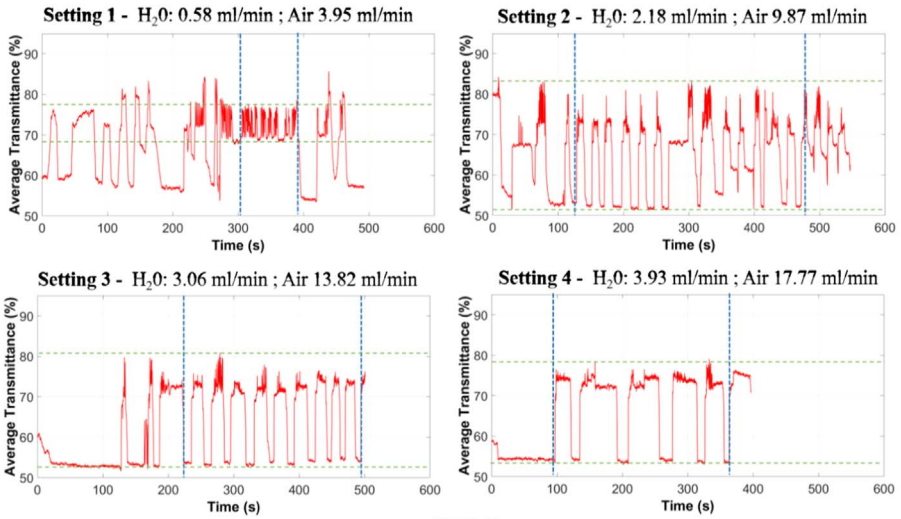

c. PTL 3

Figure 6. Time-dependent average transmission plots for (a) PTL 1, (b) PTL 2, and (c) PTL 3 and the different experimental settings of flow conditions. The vertical blue lines define the periods that are later on used for calculations.

In counter current flows, it is shown by Unsal et al.,[35] that the bubble snap-off at the inlet interface, similar to as shown in Fig. 8, could result in fluctuations of the capillary back pressure. As a result, the rate of imbibition tends to decrease in comparison to co-current flows. The dependency of invasion on the interplay of PTL-structure and flow conditions could explain the different outcomes of studies

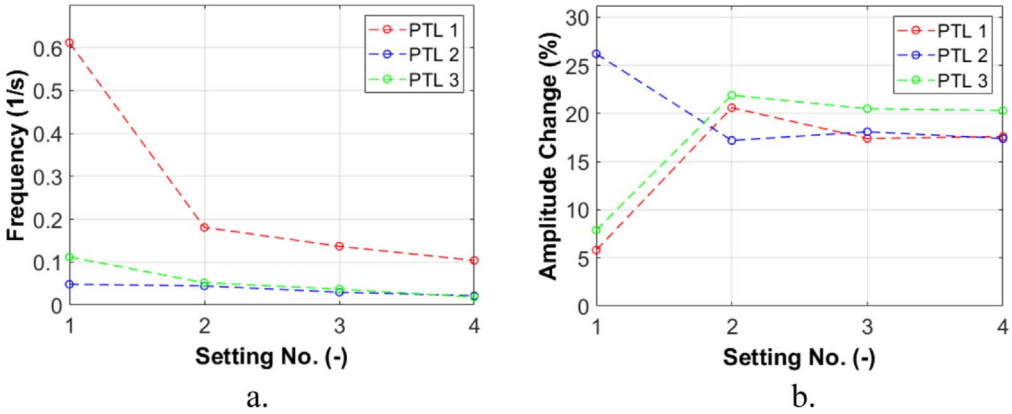

Figure 7. (a) Dependence of frequency and (b) of the amplitude of the change of the average transmission on PTL structure and flow conditions.

Table III. Analysis of the plots in Fig. 6. Average filling and drainage times along with the standard deviation as well as amplitude of the change of the average transmission value and frequency of the imbibition/drainage cycles.

	Set.	Amplitude change (%)	Time of pressure build-up (s)	Drainage time (s)	Average frequency (s^{-1})
PTL 1	1	5.8	0.9 ± 0.2	0.9 ± 0.1	0.612
	2	20.6	3.4 ± 1.8	3.1 ± 1.5	0.181
	3	17.4	2.3 ± 0.4	5.2 ± 2.9	0.137
	4	17.6	2.5 ± 0.3	7.2 ± 1.2	0.104
PTL 2	1	26.2	16.5 ± 6.8	9.8 ± 1.6	0.049
	2	17.2	13.1 ± 3.5	10.9 ± 2.3	0.045
	3	18.1	13.0 ± 2.4	20.4 ± 3.5	0.030
	4	17.4	12.6 ± 4.1	32.7 ± 7.6	0.021
PTL 3	1	7.9	4.3 ± 2.6	6.4 ± 4.8	0.112
	2	21.9	10.6 ± 2.5	10.2 ± 2.5	0.052
	3	20.5	10.3 ± 1.9	18.3 ± 2.9	0.037
	4	20.3	14.1 ± 4.6	39.1 ± 13.4	0.019

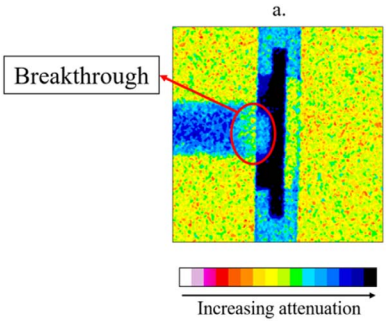

Figure 8. In-plane image taken during counter current flow in the moment when air breaks through the PTL from the gas channel side (on the right) to the water channel side (on the left). PTL in black; water in dark blue to black; gas in yellow to green; aluminum housing in yellow to green.

presented in literature, where flow conditions and structure are investigated independently of each other.[13,17,18] Basically, a better overview of the correlations of structure and flow conditions with PTL invasion would be required for a broad range of parameters (flow rates, pressure conditions and PTL morphology) to enhance the understanding of transport limitations.

Determination of breakthrough points.—The characteristics of the gas invasion can be further studied based on the breakthrough area of air. In more details, it was of interest, if the specific properties of the gas invasion were principally repeated during the drainage cycles, i.e. if the gas invasion occurred at constant position and with a constant structure. For this purpose, the water thickness, computed from Eq. 5, is plotted in Fig. 9 from the periods with quasi steady-state imbibition/drainage cycles highlighted by the blue vertical lines in Fig. 6. The breakthrough area is identified by the minima of the average water thickness from all images.

As can be seen, the breakthrough area changed for each PTL between horizontal position 3 mm and 7.6 mm but otherwise remained almost constant, i.e. independent of the flow conditions. This means, that the change of flow rates did not affect the breakthrough location. Instead, the gas invasion was repeated always at the same position.

In author's opinion, a unique breakthrough location can be explained by two main factors: i) the spatially distributed ΔP between water and air channel and ii) the pore size distribution of the PTLs. This is in accordance with findings of Seweryn et al.,[15] Zlobinski et al.,[13] and Panchenko et al.[30] who also suggested constant invasion regions.

Conclusions

In this study, mass transport in three commercial titanium fiber PTLs was investigated using in-operando neutron imaging of counter-current two-phase flow in a model cell. The investigation was conducted for different flow conditions with the aim to show that the invasion process depends on the interplay of structure with the specific fluid flow conditions.

The experiments revealed a constant periodic repetition of imbibition/drainage cycles with frequencies depending on the PTL structure and fluid flow rates. The change of the water saturation, identified from through-plane images of the flow cell, remained constant during these cycles and appeared to be almost independent of the specific PTL structures and flow rates. Only the thicker PTL 3 had a higher oxygen saturation after drainage. In summary, it can be

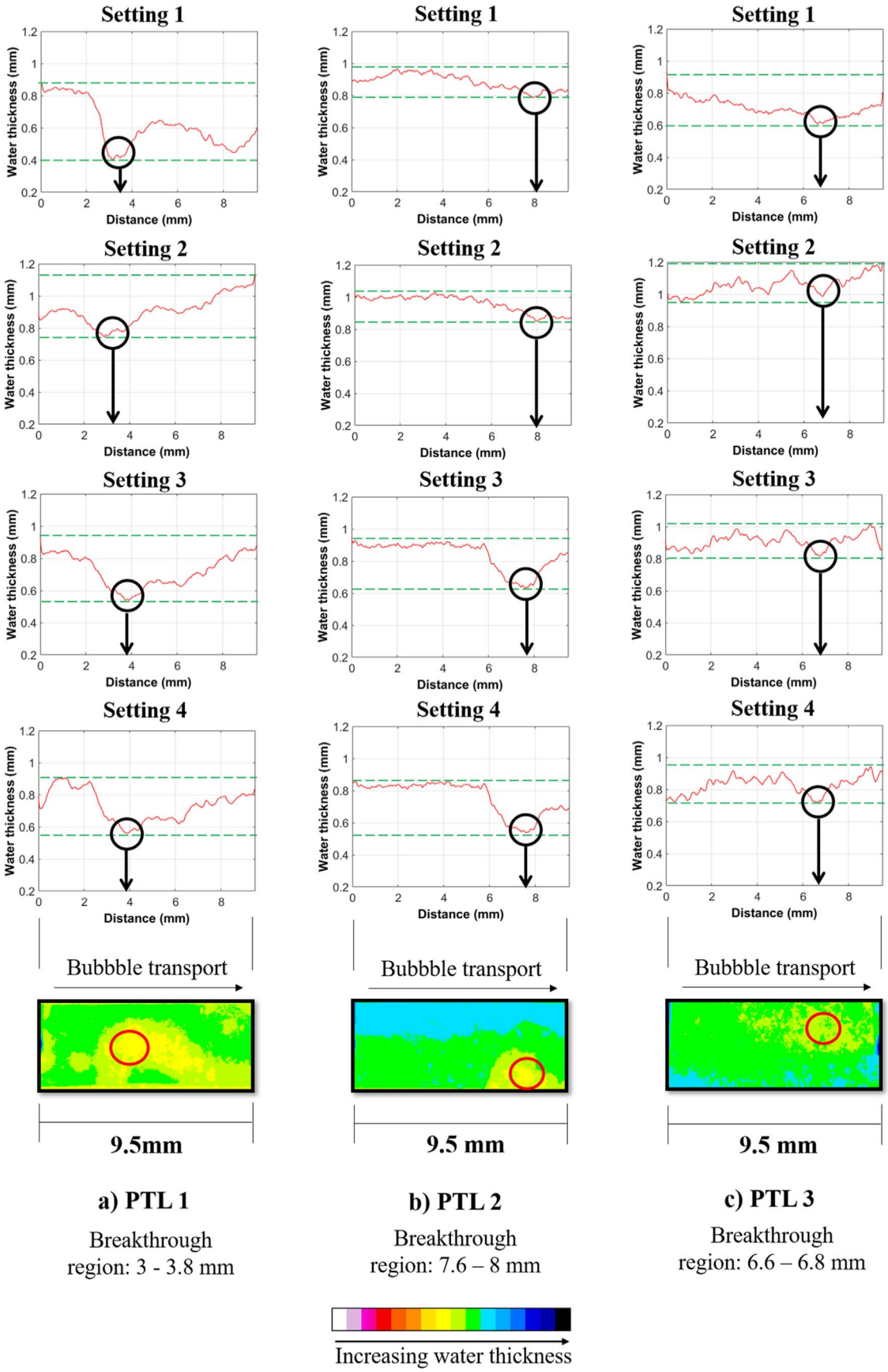

Figure 9. Breakthrough locations for each cell and setting using water thickness plots. The data is averaged over the time periods highlighted in Fig. 6, i.e. where the imbibition-drainage cycles were well repeated. In the through-plane view, the transmittance signal comprises the information of the water inside the PTL as well as the water inside the liquid supply channel, which has a thickness of 0.5 mm.

concluded that the studied PTLs with different thickness and structure have similar water retention qualities after drainage. The invasion furthermore occurred at almost constant locations in each PTL, again independent of the stoichiometry. Additionally, the invasion frequencies of PTL 1 were the highest. It was concluded that the achievable high gas pressures in case of PTL 1 could be favorable for mass transfer, especially on the gas side due to the gradient in pore sizes. For efficient transport of fluids, using fibers of different wettability have also been suggested to enhance the formation of minimal surfaces[23] and the use of 3D printed microstructures suggested for GDLs[36] could also be implemented for PTLs.

From the tomography of imbibition and drainage of PTL 2 and PTL 3, water scarcity was documented, even after repetition of several imbibition/drainage cycles. The dry regions are expected to enhance the gas flow rates, if they form an interconnected region between the top and bottom interface.

For the future work, electrochemical cells will be used in neutron imaging to study the contribution of the PTLs in the mass transport losses of an electrolyser. Different commercial PTLs will be used in these cells too. The goal will be to observe the gas/liquid distributions at different current densities and to compare the electrolyser performance based on different PTLs.

Acknowledgments

This research was supported by the International Max Planck Research School for Advanced Methods in Process and Systems Engineering (IMPRS ProEng), Magdeburg, Germany and the Center of Dynamic Systems (CDS), funded by the EU-program ERDF (European Regional Development Fund). The beamtime for this work was approved by Ni-Matters, a joint research unit comprised of the Institut Laue Langevin, the Helmholtz-Zentrum Berlin and the Université Grenoble Alpes. We would also like to express our gratitude to the beam scientists Alessandro Tengattini and Lukas Helfen for their technical assistance at the Institut Laue-Langevin, Grenoble.

ORCID

H. Altaf https://orcid.org/0000-0002-3498-092X
T. Milicic https://orcid.org/0000-0002-3227-0852
T. Vidakovic-Koch https://orcid.org/0000-0003-3896-3585
Alessandro Tengattini https://orcid.org/0000-0003-0320-3340
N. Kardjilov https://orcid.org/0000-0002-0980-1440
T. Arlt https://orcid.org/0000-0002-0715-2213
I. Manke https://orcid.org/0000-0001-9795-5345
N. Vorhauer-Huget https://orcid.org/0000-0001-5825-4984

References

1. X.-Z. Yuan, N. Shaigan, C. Song, M. Aujla, V. Neburchilov, J. T. H. Kwan, D. P. Wilkinson, A. Bazylak, and K. Fatih, *Sustainable Energy Fuels*, **6**, 1824 (2022).
2. S. A. Grigoriev, P. Millet, S. A. Volobuev, and V. N. Fateev, *Int. J. Hydrogen Energy*, **34**, 4968 (2009).
3. H. Ito, T. Maeda, A. Nakano, C. M. Hwang, M. Ishida, A. Kato, and T. Yoshida, *Int. J. Hydrogen Energy*, **37**, 7418 (2012).
4. C. Lee, B. Zhao, R. Abouatallah, R. Wang, and A. Bazylak, *Phys. Rev. Applied*, **11** 054029 (2019).
5. J. O. Majasan, F. Iacoviello, P. R. Shearing, and D. J. L. Brett, *Energy Procedia*, **151**, 111 (2018).
6. M. Carmo, D. L. Fritz, J. Mergel, and D. Stolten, *Int. J. Hydrogen Energy*, **38**, 4901 (2013).
7. H. Altaf, N. Vorhauer, E. Tsotsas, and T. Vidaković-Koch, *Processes*, **8**, 362 (2020).
8. N. Vorhauer, H. Altaf, E. Tsotsas, and T. Vidakovic-Koch, *Processes*, **7**, 558 (2019).
9. E. B. Fox, R. Héctor, and M. Colón-, *Mass Transfer*, ed. H. Nakajima (IntechOpen, Rijeka) (2011).
10. R. Lenormand, E. Touboul, and C. Zarcone, *J. Fluid Mech.*, **189**, 165 (1988).
11. Y. Li, G. Yang, S. Yu, Z. Kang, J. Mo, B. Han, D. A. Talley, and F.-Y. Zhang, *Int. J. Hydrogen Energy*, **44**, 28283 (2019).
12. T. G. Tranter, P. Boillat, A. Mularczyk, V. Manzi-Orezzoli, P. R. Shearing, D. J. L. Brett, J. Eller, J. T. Gostick, and A. Forner-Cuenca, *J. Electrochem. Soc.*, **167**, 114512 (2020).
13. M. Zlobinski, T. Schuler, F. N. Büchi, T. J. Schmidt, and P. Boillat, *J. Electrochem. Soc.*, **167**, 84509 (2020).
14. D. Wildenschild and A. P. Sheppard, *Adv. Water Res.*, **51**, 217 (2013).
15. J. Seweryn, J. Biesdorf, T. J. Schmidt, and P. Boillat, *J. Electrochem. Soc.*, **163**, F3009 (2016).
16. O. Panchenko et al., *Energies*, **12**, 350 (2019).
17. M. Maier et al., *J. Power Sources*, **455**, 227968 (2020).
18. J. K. Lee, C. Lee, K. F. Fahy, B. Zhao, J. M. LaManna, E. Baltic, D. L. Jacobson, D. S. Hussey, and A. Bazylak, *Cell Reports Physical Science*, **1**, 100147 (2020).
19. O. F. Selamet, U. Pasaogullari, D. Spernjak, D. S. Hussey, D. L. Jacobson, and M. D. Mat, *Int. J. Hydrogen Energy*, **38**, 5823 (2013).
20. P. Satjaritanun, M. O'Brien, D. Kulkarni, S. Shimpalee, C. Capuano, K. E. Ayers, N. Danilovic, D. Y. Parkinson, and I. V. Zenyuk, *iScience*, **23**, 101783 (2020).
21. P. Shrestha, D. Ouellette, J. Lee, N. Ge, A. K. C. Wong, D. Muirhead, H. Liu, R. Banerjee, and A. Bazylak, *Adv. Mater. Interfaces*, **6**, 1901157 (2019).
22. C. Zhang, M. Oostrom, T. W. Wietsma, J. W. Grate, and M. G. Warner, *Energy Fuels*, **25**, 3493 (2011).
23. M. J. Shojaei, B. Bijeljic, Y. Zhang, and M. J. Blunt, *ACS Appl. Energy Mater.*, **5**, 4613 (2022).
24. Q. Lin, B. Bijeljic, S. Berg, R. Pini, M. J. Blunt, and S. Krevor, *Phys. Rev. E*, **99**, 63105 (2019).
25. R. T. Armstrong, A. Georgiadis, H. Ott, D. Klemin, and S. Berg, *Geophys. Res. Lett.*, **41**, 55 (2014).
26. R. T. Armstrong and S. Berg, *Phys. Rev. E: Stat. Nonlinear Soft Matter Phys.*, **88**, 43010 (2013).
27. A. Ferrari and I. Lunati, *Adv. Water Res.*, **57**, 19 (2013).
28. G. Garfi, C. M. John, M. Rücker, Q. Lin, C. Spurin, S. Berg, and S. Krevor, *J. Colloid Interface Sci.*, **613**, 786 (2022).
29. M. A. Hoeh, T. Arlt, N. Kardjilov, I. Manke, J. Banhart, D. L. Fritz, J. Ehlert, W. Lüke, and W. Lehnert, *ECS Trans.*, **69**, 1135 (2015).
30. O. Panchenko et al., *J. Power Sources*, **390**, 108 (2018).
31. C. Lee, J. K. Lee, B. Zhao, K. F. Fahy, and A. Bazylak, *J. Electrochem. Soc.*, **167**, 24508 (2020).
32. A. Tengattini, N. Lenoir, E. Andò, B. Giroud, D. Atkins, J. Beaucour, and G. Viggiani, *Nucl. Instrum. Methods Phys. Res., Sect. A*, **968**, 163939 (2020).
33. J. H. Hubbell and S. M. Seltzer, *Tables of X-ray Mass Attenuation Coefficients and Mass Energy-Absorption Coefficients (version 1.4)* (National Institute of Standards and Technology, Gaithersburg, MD)(NIST Standard Reference Database 126) (2004).
34. A. Mularczyk, Q. Lin, M. J. Blunt, A. Lamibrac, F. Marone, T. J. Schmidt, F. N. Büchi, and J. Eller, *J. Electrochem. Soc.*, **167**, 84506 (2020).
35. E. Unsal, G. Mason, N. R. Morrow, and D. W. Ruth, *J. Colloid Interface Sci.*, **306**, 105 (2007).
36. D. Niblett, V. Niasar, and S. Holmes, *J. Electrochem. Soc.*, **167**, 13520 (2020).